the experimental pressure range. If oxygen solubility does increase at pressures higher than 25 GPa, this would reduce the magma ocean depth required on the Earth to satisfy the FeO content of the present-day mantle and make it more likely that oxygen remained dissolved in the metal as it formed the core.

An important consequence for the Earth is that the metal that segregated at the base of the magma ocean would have contained a significant amount of oxygen (for example, 7–8 wt%). As a result of increasing pressure, the solubility of oxygen in Fe-alloy is predicted to decrease with depth below the magma ocean (Fig. 2). There are three possibilities for the fate of the dissolved oxygen, all of which could be important. (1) FeO precipitated from liquid metal between the base of the magma ocean and the proto-core, thus creating chemical heterogeneities that may still exist in the lowermost mantle[8]. (2) Oxygen was transported by liquid metal to the core, where FeO precipitated to form the D″ layer at the core–mantle boundary[9]. (3) At least part of the oxygen may still be dissolved in the core (up to 8 wt% according to our model), thus contributing significantly to its light-element budget[10,11]. If oxygen does become more soluble in liquid metal at pressures higher than our experimental conditions, then that would tend to favour this final possibility. In contrast, the martian core is unlikely to contain any dissolved oxygen, which is consistent with its probable high sulphur content[7]. □

Received 6 October 2003; accepted 8 March 2004; doi:10.1038/nature02473.

1. Li, J. & Agee, C. B. Geochemistry of mantle–core differentiation at high pressure. *Nature* **381,** 686–689 (1996).
2. Li, J. & Agee, C. B. The effect of pressure, temperature, oxygen fugacity and composition on partitioning of nickel and cobalt between liquid Fe-Ni-S alloy and liquid silicate: Implications for the Earth's core formation. *Geochim. Cosmochim. Acta* **65,** 1821–1832 (2001).
3. Righter, K., Drake, M. J. & Yaxley, G. Prediction of siderophile element/silicate partition coefficients to 20 GPa and 2800 °C: the effects of pressure, temperature, oxygen fugacity, and silicate and metallic melt compositions. *Phys. Earth Planet. Inter.* **100,** 115–134 (1997).
4. Righter, K., Hervig, R. L. & Kring, D. A. Accretion and core formation on Mars: molybdenum contents of melt inclusion glasses in three SNC meteorites. *Geochim. Cosmochim. Acta* **62,** 2167–2177 (1998).
5. Anderson, D. L. *Theory of the Earth* (Blackwell, Boston, 1989).
6. Dreibus, G. & Wanke, H. Mars, a volatile-rich planet. *Meteoritics* **20,** 367–381 (1985).
7. McSween, H. Y. Jr What we have learnt about Mars from SNC meteorites. *Meteoritics* **29,** 757–779 (1994).
8. Kellogg, L. H., Hager, B. H. & van der Hilst, R. D. Compositional stratification in the deep mantle. *Science* **283,** 1881–1884 (1999).
9. Garnero, E. J., Revenaugh, J., Williams, Q., Lay, T. & Kellogg, L. H. in *The Core-Mantle Boundary Region* (eds Gurnis, M., Wysession, M. E., Knittle, E. & Buffett, B. A.) 319–334 (Geodynamics Series 28, Am. Geophys. Union, Washington, 1998).
10. Poirier, J.-P. Light elements in the Earth's outer core: A critical review. *Phys. Earth Planet. Inter.* **85,** 319–337 (1994).
11. Hillgren, V., Gessmann, C. K. & Li, J. in *Origin of the Earth and Moon* (eds Canup, R. & Righter, K.) 245–263 (Univ. Arizona Press, Tucson, 2000).
12. Melosh, H. J. in *Origin of the Earth* (eds Newsom, H. E. & Jones, J. H.) 69–83 (Oxford Univ. Press, Oxford, 1990).
13. Stevenson, D. J. in *Origin of the Earth* (eds Newsom, H. E. & Jones, J. H.) 231–249 (Oxford Univ. Press, Oxford, 1990).
14. Gessmann, C. K. & Rubie, D. C. The effect of temperature on the partitioning of Ni, Co, Mn, Cr and V at 9 GPa and constraints on formation of the Earth's core. *Geochim. Cosmochim. Acta* **62,** 867–882 (1998).
15. O'Neill, H. S. C., Canil, D. & Rubie, D. C. Metal-oxide equilibria to 2500 °C and 25 GPa: implications for core formation and the light component in the Earth's core. *J. Geophys. Res.* **103,** 12239–12260 (1998).
16. Kato, T. & Ringwood, A. E. Melting relationships in the system Fe-FeO at high pressures: implications for the composition and formation of the Earth's core. *Phys. Chem. Miner.* **16,** 524–538 (1989).
17. Trønnes, R. G. Melting relations and major element partitioning in an oxidized bulk Earth model composition at 15–26 GPa. *Lithos* **53,** 233–245 (2000).
18. Trønnes, R. G. & Frost, D. J. Peridotite melting and mineral-melt partitioning of major and minor elements at 22–24.5 GPa. *Earth Planet. Sci. Lett.* **197,** 117–131 (2002).
19. Li, J. & Agee, C. B. Element partitioning constraints on the light element composition of the Earth's core. *Geophys. Res. Lett.* **28,** 81–84 (2001).
20. Rubie, D. C., Melosh, H. J., Reid, J. E., Liebske, C. & Righter, K. Mechanisms of metal-silicate equilibration in the terrestrial magma ocean. *Earth Planet. Sci. Lett.* **205,** 239–255 (2003).
21. Herzberg, C. & Zhang, J. Melting experiments on anhydrous peridotite KLB-1: Compositions of magmas in the upper mantle and transition zone. *J. Geophys. Res.* **101,** 8271–8295 (1996).
22. Ohtani, E. Melting temperature distribution and fractionation in the lower mantle. *Phys. Earth Planet. Inter.* **33,** 12–25 (1983).
23. McDonough, W. F. & Sun, S.-s. The composition of the Earth. *Chem. Geol.* **120,** 223–253 (1995).
24. O'Neill, H. S. C. & Palme, H. in *The Earth's Mantle* (ed. Jackson, I.) 3–126 (Cambridge Univ. Press, Cambridge, 1998).
25. Chabot, N. L. & Agee, C. B. Core formation in the Earth and Moon: new experimental constraints from V, Cr and Mn. *Geochim. Cosmochim. Acta* **67,** 2077–2091 (2003).
26. Gessmann, C. K. & Rubie, D. C. The origin of the depletions of V, Cr, and Mn in the mantles of the Earth and Moon. *Earth Planet. Sci. Inter.* **184,** 95–107 (2000).
27. Bouhifd, M. A. & Jephcoat, A. P. The effect of pressure on partitioning of Ni and Co between silicate and iron-rich metal liquids: a diamond-anvil cell study. *Earth Planet. Sci. Inter.* **209,** 245–255 (2003).
28. Chase, M. W. J. *et al.* JANAF thermochemical tables. *J. Phys. Chem. Ref. Data* **14** (suppl. 1) (1985).
29. Sundman, B. An assessment of the Fe-O system. *J. Phase Equil.* **12,** 127–140 (1991).
30. Fei, Y. & Mao, H.-K. In situ determination of the NiAs phase of FeO at high pressure and temperature. *Science* **266,** 1678–1680 (1994).

Supplementary Information accompanies the paper on **www.nature.com/nature**.

Acknowledgements We thank H. Fischer, G. Herrmannsdörfer, D. Krausse and H. Schulze for technical assistance. The German Science Foundation (DFG) supported this research.

Competing interests statement The authors declare that they have no competing financial interests.

Correspondence and requests for materials should be addressed to D.C.R. (dave.rubie@uni-bayreuth.de).

Convergent evolution in mechanical design of lamnid sharks and tunas

Jeanine M. Donley[1], Chugey A. Sepulveda[1], Peter Konstantinidis[2], Sven Gemballa[2] & Robert E. Shadwick[1]

[1]*Marine Biology Research Division, Scripps Institution of Oceanography, University of California San Diego, La Jolla, California 92093-0202, USA*
[2]*Department of Zoology, University of Tübingen, Auf der Morgenstelle 28, D-72076 Tübingen, Germany*

The evolution of 'thunniform' body shapes in several different groups of vertebrates, including whales, ichthyosaurs[1] and several species of large pelagic fishes[2] supports the view that physical and hydromechanical demands provided important selection pressures to optimize body design for locomotion during vertebrate evolution. Recognition of morphological similarities between lamnid sharks (the most well known being the great white and the mako) and tunas has led to a general expectation that they also have converged in their functional design; however, no quantitative data exist on the mechanical performance of the locomotor system in lamnid sharks. Here we examine the swimming kinematics, *in vivo* muscle dynamics and functional morphology of the force-transmission system in a lamnid shark, and show that the evolutionary convergence in body shape and mechanical design between the distantly related lamnids and tunas is much more than skin deep; it extends to the depths of the myotendinous architecture and the mechanical basis for propulsive movements. We demonstrate that not only have lamnids and tunas converged to a much greater extent than previously known, but they have also developed morphological and functional adaptations in their locomotor systems that are unlike virtually all other fishes.

During their 400 million years of independent evolution, sharks and bony fishes have diverged in many fundamental aspects of their anatomy and physiology. However, two groups of dominant open-ocean predators, the lamnid sharks and the tunas, even when looked at superficially, display remarkably similar morphological specializations related to locomotion[3–12] (Fig. 1a). The shared characteristics in these distantly related groups that distinguish them from virtually all other fish have arisen independently, probably as the result of selection for fast and continuous locomotion. Moreover, in both lamnids and tunas, the aerobic (red) musculature that powers cruise swimming is concentrated in a more medial (closer to the

backbone) and anterior position compared with the relatively uniform and superficial position in other fishes; the body temperature is elevated above that of the surrounding water, facilitated by counter-current heat exchangers associated with the internal red muscle; and the muscle segments (myotomes) are highly elongated[3].

Recent studies on tunas revealed a host of unique functional adaptations in their locomotor system that distinguish tunas from all other bony fishes[4,13]. Similar investigations on swimming lamnid sharks are lacking because of the difficulty in handling such large and dangerous predators; thus, the dynamic properties of the lamnid locomotor system remain unknown. This paper presents *in vivo* quantitative measurements of swimming kinematics and muscle dynamics, and analysis of the morphology of the force-transmission system in a lamnid shark.

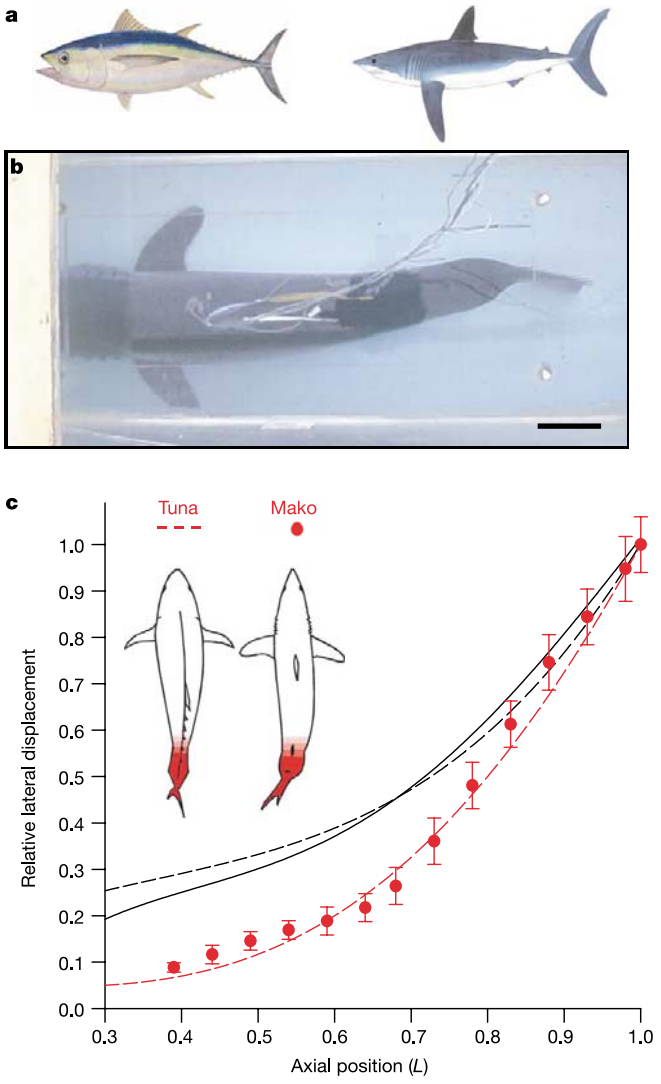

Figure 1 Features of thunniform body shape and patterns of lateral undulation during steady swimming. **a**, Thunniform body shape in lamnid sharks[25] (right) and tunas[26] (left). Note the highly streamlined fusiform body shape that minimizes pressure drag, stiff, high-aspect-ratio hydrofoil caudal fin that produces thrust by a hydrodynamic-lift mechanism, and dorsoventrally flattened and enlarged caudal keel that decreases drag produced by lateral movement of the peduncle[6–8]. **b**, Dorsal image of steady swimming *I. oxyrinchus*. Scale bar: 10 cm. **c**, Lateral displacement, relative to the amplitude of lateral motion at the tail tip, versus axial position in the mako shark ($n = 5$; red symbols), tuna (red dashed line[27]), leopard shark (black solid line[15]) and subcarangiform teleosts (black dashed line; modified from ref. 13). This graph emphasizes differences in displacement in the mid-body where most of the variation among swimming modes occurs. Comparison of the mako shark and tuna illustrates the similarity in their swimming mode, where lateral undulations are largely confined to the caudal region, indicated by shading in dorsal outlines. The reduction in lateral motion in the mid-body region afforded by their internal red muscle and modified force-transmission system is evident when comparing the mako shark and tuna to sharks and bony fishes with less-specialized swimming modes such as the subcarangiforms shown here.

First, we examined the kinematics of steady swimming in the shortfin mako shark (*Isurus oxyrinchus*). Lateral displacement of the dorsal midline as a function of body position was calculated from dorsal video images of mako sharks swimming under controlled conditions in a swim tunnel (Fig. 1b; see also Supplementary Video). Descriptions of undulatory swimming modes in fishes are based on the proportion of the body that participates in the lateral thrust-producing movements[14], and can be distinguished by differences in patterns of lateral displacement along the body, as shown in Fig. 1c. Compared with other teleosts, tunas exhibit the least undulatory (thunniform) mode of locomotion, in which lateral movements are largely confined to the caudal region where body mass is reduced by tapering. The lateral displacement data presented here show that the lamnid shark kinematically resembles tuna more than other sharks[15] or subcarangiform teleosts: the degree of lateral motion along the mako shark's body from ~0.4*L* to ~0.8*L* (where *L* is total body length) is relatively small, demonstrating that lamnids swim using a thunniform-like mode. The amplitude of lateral motion increases substantially beyond ~0.8*L* where the body tapers to the narrow caudal peduncle. Lamnids, like tunas, have the least lateral motion in the mid-body region where the bulk of the muscle resides and have a reduced body mass in the caudal region where lateral amplitudes are high, both being features that match predictions for enhancing hydromechanical efficiency of swimming[9].

Because lamnids have both internal red muscle and a thunniform-like swimming mode, we tested the possibility that shortening of the red muscle would be physically uncoupled from deformation of the adjacent skin, backbone and white muscle, a unique functional property of red muscle that has been observed so far only in tunas. Whereas in most teleosts superficial red muscle fibres contract sequentially to cause a posteriorly travelling wave of local body bending[16–18], the internal position of red muscle in tunas allows them to abandon this pattern of undulation and adopt a novel mechanism to project red muscle action to posterior regions of the body[4,19], thereby facilitating thunniform kinematics. In the mako shark we used sonomicrometry to record instantaneous muscle segment length changes during steady swimming as well as during passive, simulated swimming movements induced under anaesthesia. The temporal relationship between red and white muscle shortening was measured to determine whether the action of these two muscle masses is synchronized, as in most fish, or uncoupled, as in tunas. During passive swimming movements, peaks in red muscle strain (that is, relative length change) were in phase with peaks in adjacent white muscle strain (Fig. 2a). Thus, when the body bends passively red muscle shortens synchronously with the surrounding white muscle and skin, as one would expect. In contrast, during active swimming the peaks in red muscle strain were delayed relative to peaks in white muscle strain (Fig. 2b). By cross-correlation analysis we determined that the mean phase shift between simultaneous recordings of red and white muscle strain was 90 ms (or ~10% of the tail-beat cycle), with one individual as high as 174 ms (~17% of tail-beat cycle). The observed phase shift indicates that during steady swimming the red muscle is indeed physically uncoupled from the surrounding tissues and contracts in phase with body bending at a more posterior location.

On the basis of a wave velocity of about $1\,l\,s^{-1}$ in sharks swimming with a tail-beat frequency of about 1 Hz, the red muscle in the mid-body region will be shortening in phase with bending of the backbone 10–17% closer to the tail. A consequence is that

during short portions of each contraction cycle the red muscle will be lengthening while the adjacent white fibres are shortening, and vice versa. The loose sheath of connective tissue that surrounds the red muscle mass (see Fig. 3d) may facilitate this shearing. These results are remarkably similar to those described in tunas, where the deep red muscle shortens and transmits force and displacement to more posterior regions of the body rather than effecting local bending[4,19]. Thus, the same mechanism enables tunas and lamnid sharks to swim with the relatively stiff-bodied thunniform mode of propulsion; even though the bulk of aerobic muscle is located more

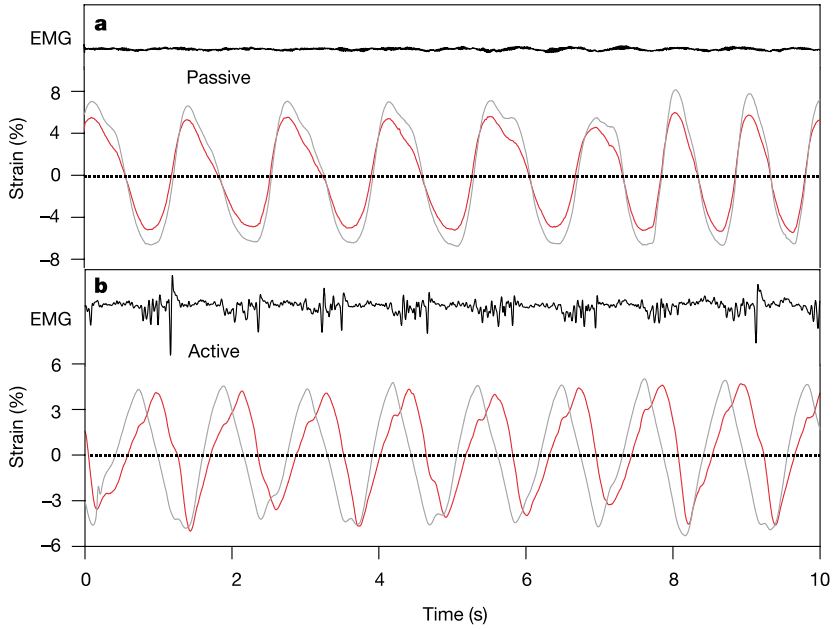

Figure 2 Simultaneous recordings of muscle strain (segment length change/mean length) of red (red trace) and adjacent white (grey trace) muscle during passive simulated swimming movements (**a**) and active steady swimming ($0.5\,l\,s^{-1}$) (**b**) in the mako shark. During active swimming, as verified by red muscle activity (EMG trace), shortening in the red muscle is delayed relative to the white muscle and is therefore in phase with lateral motion in more posterior positions.

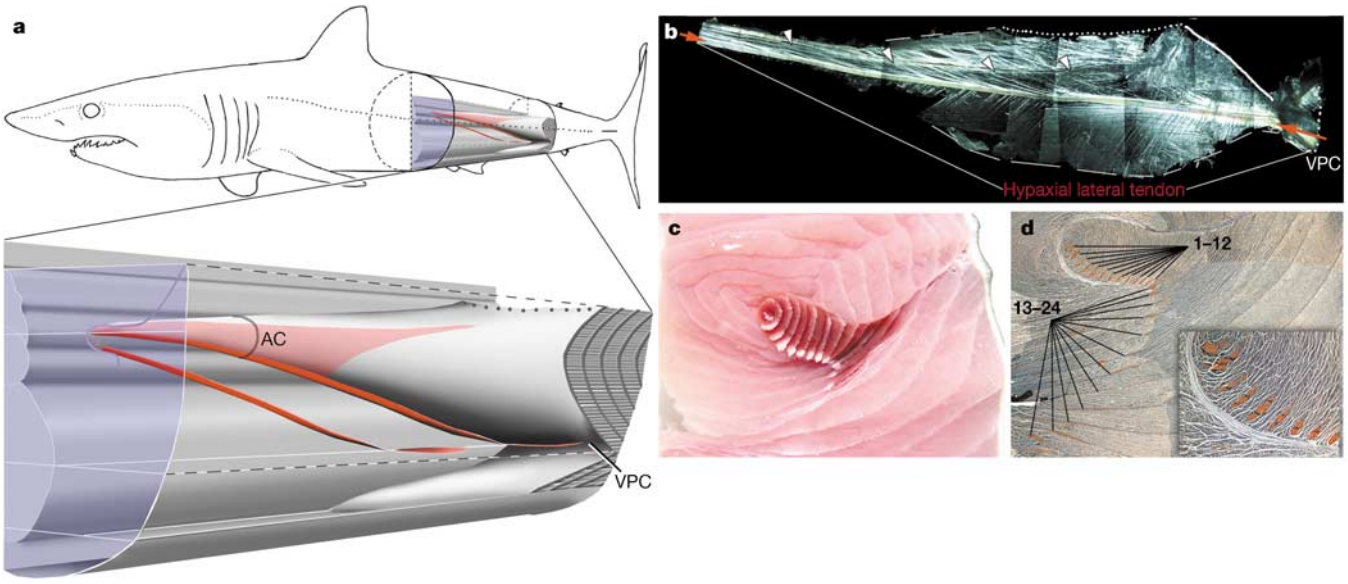

Figure 3 Collagenous architecture of myosepta of *I. oxyrinchus*. **a**, Oblique view focusing on the hypaxial part between 0.54*L* and 0.74*L* (coloured inset). The elongated anterior pointing cone (AC) of one myoseptum is shown. It intersects with the red musculature (pale red area) and contains the hypaxial lateral tendon (dark red). The hypaxial lateral tendon extends between the tip of the anterior pointing cone and the ventral posterior cone (VPC). The hypaxial lateral tendon of a more anterior myoseptum is also shown without its myoseptal sheet. The anterior part of this tendon is cut at its intersection with the transverse plane (blue). **b**, Excised area of myosepta between the anterior pointing cone and ventral posterior cone flattened out under polarized light. Pathways of collagenous structures are shown in white. The hypaxial lateral tendon extends between the red arrows. Dashed line, excision line from vertebral axis; thick white line, excision line from skin; dotted line, excision line from remaining dorsal part of the myosepta, equivalent to the dotted line in **a**; white arrowheads, intersection line of myosepta and loose connective tissue surrounding red muscle. **c**, **d**, Transverse sections of left side. Concentric rings of myosepta indicate nesting anterior pointing cones. **c**, Fresh section, 0.6*L*, showing red muscle with sections of hypaxial lateral tendons (white) within the red muscle. **d**, Histological section at 0.54*L*. Red muscle is separated from surrounding white muscle by a sheath of loose connective tissue. Numbers 1–12 indicate anterior portions of 12 hypaxial lateral tendons present in red muscle, whereas numbers 13–24 indicate posterior portions of 12 additional hypaxial lateral tendons present in white muscle, meaning that a single tendon covers 24 segments. The inset shows a detailed view of red muscle and hypaxial lateral tendons (stained orange).

anteriorly than in less derived species, the lateral motion it produces is primarily focused to the caudal region.

Our morphological investigations demonstrate that the anatomical specializations associated with the force-transmission system are also convergent. We used a new combination of techniques to explore the three-dimensional morphology of the tendinous connective tissue linkages (myosepta) that transmit muscular forces to the skin and backbone, and their relationship to the internal red muscle in the mako shark.

In principle, the three-dimensional shape of myotomes and their associated myosepta in mako sharks resembles the regular pattern in gnathostome fishes[20], which includes a main anterior cone and a dorsal and ventral posterior cone (see Supplementary Fig. 1 for myoseptal parts of gnathostomes and mako sharks). Additionally, in mako sharks two secondary anterior cones are present at the dorsal- and ventral-most part of the myoseptum. The red muscle is situated in the lower part of the main anterior cone (Fig. 3a; see also Supplementary Fig. 1d, e) where its fibres insert into the collagenous myoseptum. In particular, red muscle fibres insert into the anterior half of a myoseptal tendon (Fig. 3a). This tendon runs from the tip of the main anterior cone through the red muscle towards its end within the white muscle at the ventral posterior cone (Fig. 3a, b). It clearly represents the homologue of the hypaxial lateral tendon in gnathostome fishes (Supplementary Fig. 1). In mako sharks, this tendon is extremely prominent and elongated when compared with other fishes. In fact, myoseptal tendons as long and as distinct as those associated with the red muscle in the mako shark have never been reported in any shark species. We measured tendon lengths as long as 0.19*L* in the posterior region of the body (Supplementary Fig. 1e). The sonomicrometric results suggest that the action of the red muscle is directed posteriorly along the body by 10–17%. The measured tendon lengths accord well with the values predicted from sonomicrometry, suggesting that the hypaxial lateral tendon is responsible for transmitting red muscle forces posteriorly. The prominent tendons of the posterior body are gradually developed along a rostrocaudal gradient from shorter (~0.06*L*; Supplementary Fig. 1d) and less distinct hypaxial lateral tendons of anterior myosepta to longer tendons in the posterior.

In tunas, distinct and elongated tendons have also been discovered and have been hypothesized to transfer forces from the red muscle to the axial skeleton, and thus provide the anatomical basis for force transmission from the anterior to the caudal region[21]. As in mako sharks, the available length measurements and sonomicrometric data are in good accordance (0.18*L* experimentally and 0.16*L* morphologically)[22]. Although in tunas the primary force-transmitting tendons are in the horizontal septum, in the mako shark, as in other sharks[23], we found the horizontal septum to be reduced in the posterior half of the body. Instead, the primary linkage to the tail appears to be the hypaxial lateral tendons. Interestingly, although the posterior oblique tendons in tunas and hypaxial lateral tendons in mako sharks provide the same function, they have different anatomical origins.

Through distinct evolutionary pathways lamnid sharks and tunas have converged on the same mechanical design principle, that of having internalized red muscle associated with a highly derived force-transmission system, two features that form the basis for their thunniform swimming mode. Our study shows that not only have the physical demands of the external environment sculpted the body shapes of large pelagic cruisers, but also the internal physiology and morphology of their complex locomotor systems has been fine-tuned over the course of their evolution. □

Methods

Shortfin mako sharks (*I. oxyrinchus*, family Lamnidae) ranging in size from 80 to 112 cm *L* (total body length) were collected by hook and line off the coast of Southern California and transported to the laboratory facilities at Scripps Institution of Oceanography (SIO) in a transport chamber equipped with circulating aerated sea water. Once at SIO, the sharks were placed into a large 3,000-l swim tunnel for an acclimation period of several hours before experimentation. All procedures in capture, maintenance and experimentation followed the guidelines of the University of California, San Diego Institutional Animal Care and Use Committee.

In vivo muscle dynamics

To examine the dynamics of red and white muscle contractions during swimming, we used electromyography (EMG) and sonomicrometry, a technique for measuring distances in which piezoelectric crystals transmit and receive ultrasonic pulses. Pairs of sonomicrometric crystals were implanted into the deep red and adjacent white muscle to record instantaneous changes in muscle segment length (strain) during active periods of steady swimming as well as during passive, simulated swimming movements induced under anaesthesia. Surgery was performed on anaesthetized individuals partially submerged in a seawater bath according to procedures described previously[15]. Crystal pairs were implanted approximately 15 mm apart along the longitudinal axis of the body and the leads were loosely anchored to the skin with surgical sutures. To verify the passive and active states of the red muscle, electrical activity was recorded using pairs of electrodes implanted approximately 2 mm apart directly bisecting the crystal pairs. After surgery, the sharks were placed into the swim tunnel and allowed to recover before data collection. In the recovery period we recorded red and white muscle strain during passive, simulated swimming movements induced by gentle side-to-side motions of the centre of mass that generated body undulation. Additionally, we recorded and analysed 30–50 consecutive tail-beat cycles for each individual while the shark swam steadily at approximately $0.5\,l\,s^{-1}$. To measure the relative timing of red and white muscle strain (phase shift), a cross-correlation analysis was performed using waveforms containing approximately ten consecutive tail-beat cycles. Mean phase shift presented in the text represents a mean of five individuals. Sonomicrometric and EMG signals were recorded at 500 Hz.

To correlate measurements of local muscle activation and strain with patterns of body bending, five mako sharks were videotaped while swimming against a current of known velocity in the swim tunnel. To synchronize the collection of sonomicrometric, EMG and video recordings, a flashing red diode was recorded in the video sequences and its excitation voltage was recorded with the sonomicrometric and EMG data. Kinematic analysis follows procedures described previously[15,24].

Morphology

We used a combination of clearing and staining, microdissection, polarized light microscopy, standard histology and computer-based three-dimensional reconstruction to explore the three-dimensional morphology of the tendinous connective tissue linkages (myosepta). A small body segment (0.54–0.55*L*) of a formalin-fixed mako specimen (65 cm total length) was prepared for standard histology (paraffin embedding; Azan–Domagk staining, slice thickness of 15 μm). The two remaining parts (0–0.54*L* and 0.55–1.00*L*) were carefully skinned, stained for cartilage with Alcian blue 8GX (Merck) and then cleared according to a recently described procedure[20]. Microdissections on the myoseptal system were carried out using fine microsurgery tools. Myosepta or parts of myosepta from all body regions were removed subsequently. Three-dimensional shape of the myosepta was documented by a camera lucida, and tendon lengths and rostrocaudal extensions of complete myosepta were measured *in situ*. Removed myosepta were photographed under polarized light to visualize the collagen fibre pathways and tendons (Zeiss Stemi 2000C with Fuji X digital camera HC300Z; 1,000 × 1,450 pixels). Additionally, the distribution of red muscle and its relation to myoseptal cones along the body was examined. A three-dimensional reconstruction was obtained from histological sections. Major landmarks (vertebrae, neural arches, vertical septum, abdominal cavity, tip of main anterior, secondary anterior and ventral posterior cone, sections of tendons, position of red muscle) were digitized and aligned using SurfDriver 3.5.3. Maxon Cinema 4D (Release 6) was used for choosing an adequate perspective and rendering. The obtained three-dimensional view was edited by Adobe Photoshop (final shading, adding of myoseptal shape).

Received 23 January; accepted 25 February 2004; doi:10.1038/nature02435.

1. Motani, R. Scaling effects in caudal fin propulsion and the speed of ichthyosaurs. *Nature* **415,** 309–312 (2002).
2. Lindsey, C. C. in *Fish Physiology* Vol. VII *Locomotion* (eds Hoar, W. S. & Randall, D. J.) 1–100 (Academic, New York, 1978).
3. Bernal, D., Dickson, K. A., Shadwick, R. E. & Graham, J. B. Analysis of the evolutionary convergence for high performance swimming in lamnid sharks and tunas. *Comp. Biochem. Physiol.* **129,** 695–726 (2001).
4. Katz, S. L., Syme, D. A. & Shadwick, R. E. High speed swimming: enhanced power in yellowfin tuna. *Nature* **410,** 770–771 (2001).
5. Carey, F. G., Teal, J. M., Kanwisher, J. W., Lawson, K. D. & Beckett, J. S. Warm-bodied fish. *Am. Zool.* **11,** 137–143 (1971).
6. Carey, F. G., Casey, J. G., Pratt, H. L., Urquhart, D. & McCosker, J. E. Temperature, heat production and heat exchange in lamnid sharks. *Mem. S. Calif. Acad. Sci.* **9,** 92–108 (1985).
7. Collette, B. B. in *The Physiological Ecology of Tunas* (eds Sharp, G. D. & Dizon, A. E.) 7–40 (Academic, New York, 1978).
8. Graham, J. B. & Dickson, K. A. The evolution of thunniform locomotion and heat conservation in scombrid fishes: new insights based on the morphology of *Allothunnus fallai*. *Zool. J. Linn. Soc.* **129,** 419–466 (2000).
9. Lighthill, M. J. Hydromechanics of aquatic animal propulsion—a survey. *Annu. Rev. Fluid Mech.* **1,** 413–446 (1969).
10. Magnuson, J. J. in *Fish Physiology* Vol. VII *Locomotion* (eds Hoar, W. S. & Randall, D. J.) 239–313 (Academic, New York, 1978).

11. Reif, W. E. & Weishampel, D. B. Anatomy and mechanics of the lunate tail in lamnid sharks. *Zool. Jb. Anat.* **114,** 221–234 (1986).
12. Sfakiotakis, M., Lane, D. M. & Davies, J. B. C. Review of fish swimming modes for aquatic locomotion. *J. Ocean. Eng.* **24,** 237–252 (1999).
13. Altringham, J. D. & Shadwick, R. E. in *Tuna: Physiological Ecology and Evolution* (eds Block, B. A. & Stevens, E. D.) 313–344 (Academic, San Diego, 2001).
14. Webb, P. W. Hydrodynamics and energetics of fish propulsion. *Bull. Fish. Res. Bd Can.* **190,** 1–159 (1975).
15. Donley, J. M. & Shadwick, R. E. Steady swimming muscle dynamics in the leopard shark *Triakis semifasciata*. *J. Exp. Biol.* **206,** 1117–1126 (2003).
16. Coughlin, D. J., Valdes, L. & Rome, L. C. Muscle length changes during swimming in scup: sonomicrometry verifies the anatomical high-speed cine technique. *J. Exp. Biol.* **199,** 459–463 (1996).
17. Katz, S. L., Shadwick, R. E. & Rapoport, H. S. Muscle strain histories in swimming milkfish in steady and sprinting gaits. *J. Exp. Biol.* **202,** 529–541 (1999).
18. Shadwick, R. E., Steffenson, J. F., Katz, S. L. & Knower, T. Muscle dynamics in fish during steady swimming. *Am. Zool.* **38,** 755–770 (1998).
19. Shadwick, R. E., Katz, S. L., Korsmeyer, K., Knower, T. & Covell, J. W. Muscle dynamics in skipjack tuna *Katsuwonus pelamus*: timing of red muscle shortening and body curvature during steady swimming. *J. Exp. Biol.* **202,** 2139–2150 (1999).
20. Gemballa, S. *et al.* Evolutionary transformations of myoseptal tendons in gnathostomes. *Proc. R. Soc. Lond. B* **270,** 1229–1235 (2003).
21. Westneat, M. W., Hoese, W., Pell, C. A. & Wainwright, S. A. The horizontal septum: mechanisms of force transfer in locomotion of scombrid fishes (Scombridae, Perciformes). *J. Morphol.* **217,** 183–204 (1993).
22. Katz, S. L. Design of heterothermic muscle in fish. *J. Exp. Biol.* **205,** 2251–2266 (2002).
23. Gemballa, S., Hagen, K., Röder, K., Rolf, M. & Treiber, K. Structure and evolution of the horizontal septum in vertebrates. *J. Evol. Biol.* **16,** 966–975 (2003).
24. Jayne, B. C. & Lauder, G. V. Speed effects on midline kinematics during steady undulatory swimming in largemouth bass, *Micropterus salmoides*. *J. Exp. Biol.* **198,** 585–602 (1995).
25. Compagno, L. J. V. in *FAO Identification Guide for Fishery Purposes. The Living Marine Resources of the Western Central Pacific* (eds Carpenter, K. E. & Niem, V. H.) 1274–1278 (FAO, Rome, 1998).
26. Joseph, J., Klawe, W. & Murphey, P. *Tuna and Billfish—Fish Without A Country* 1–69 (Inter-American Tropical Tuna Commission, La Jolla, California, 1988).
27. Knower, T. *Biomechanics of Thunniform Swimming* Thesis, Univ. California, San Diego (1998).

Supplementary Information accompanies the paper on **www.nature.com/nature**.

Acknowledgements We thank A. Biewener, J. Gosline, J. B. Graham, S. Vogel and N. Holland for discussion and reviews. Funding was provided by NSF and UC Regents.

Competing interests statement The authors declare that they have no competing financial interests.

Correspondence and requests for materials should be addressed to J.D. (jdonley@ucsd.edu).

Female mating bias results in conflicting sex-specific offspring fitness

Kenneth M. Fedorka* & Timothy A. Mousseau

Department of Biological Sciences, University of South Carolina, Columbia, South Carolina 29208, USA

* Present address: Department of Genetics, University of Georgia, Athens, Georgia 30602, USA

Indirect-benefit models of sexual selection assert that females gain heritable offspring advantages through a mating bias for males of superior genetic quality. This has generally been tested by associating a simple morphological quality indicator (for example, bird tail length) with offspring viability[1]. However, selection acts simultaneously on many characters, limiting the ability to detect significant associations, especially if the simple indicator is weakly correlated to male fitness[2,3]. Furthermore, recent conceptual developments suggest that the benefits gained from such mating biases may be sex-specific because of sexually antagonistic genes that differentially influence male and female reproductive ability[4]. A more suitable test of the indirect-benefit model would examine associations between an aggregate quality indicator[1,3] (such as male mating success) and gender-specific adult fitness components, under the expectation that these components may trade off[1]. Here, we show that a father's mating success in the cricket, *Allonemobius socius*, is positively genetically correlated with his son's mating success but negatively with his daughter's reproductive success. This provides empirical evidence that a female mating bias can result in sexually antagonistic offspring fitness.

With the exception of genetic monogamy, the sexes are expected to possess different optimal reproductive phenotypes[5,6]. Therefore, a conflict may arise because the sexes represent different environments in which homologous fitness-related traits are expressed[4]. Without the added evolution of sex-limited expression (that is, sexual dimorphism), sexual conflict of this nature may constrain the realization of fitness optima[6]. Unfortunately, evidence for this type of conflict is rare. However, recent empirical work in *Drosophila melanogaster* showed that adult relative fitness was negatively correlated between the sexes, even though there was a positive genetic correlation for fitness earlier in development[4]. The authors[4] further predicted that if these results were applicable outside *Drosophila*, a female mating bias for high-quality mates would produce at best only average-quality daughters.

We addressed this prediction in *A. socius* by examining the genetic correlation between a sire's field-determined mating success and his son's mating success and daughter's reproductive success. We chose these offspring variables on the assumption that they are accurate predictors of next-generation fitness. Previous work suggests that *A. socius* females mate with larger males to gain a larger haemolymph-based nuptial gift. This gift is obtained by chewing a specialized spur on the male hind tibia during copulation[7,8]. Therefore, the condition of the spur (chewed or unchewed) indicates a male's mating history (successful or unsuccessful): chewing behaviour is rarely uncoupled from sperm transfer. Spur condition also seems to be age-independent because spur categories persist throughout a breeding season that is characterized by little new male recruitment once a cohort emerges[8]. Use of an 'aggregate' indicator, such as mating success, is important because it represents the sum of interacting male traits[9], overcoming the implicit weakness of the traditional 'simple' indicator approach[1–3].

To estimate the sire–offspring correlations, we mated 47 wild-caught sires (25 successful and 22 unsuccessful) to 98 wild-caught females and reared their offspring. Sires were caught mid-breeding season and females were collected as late instar nymphs earlier in the season to ensure their virginity; on average there were two females per sire. Males that had mated in the field were larger than unmated males ($F_{1,45} = 7.25$, $P = 0.0099$) and there was no female size difference between sire groups ($F_{1,96} = 0.01$, $P = 0.9294$). From each female family, two or three sons ($n = 220$ total males) were separately placed into a mating arena with a randomly chosen, unrelated male and female taken from other sire families (see

Table 1 **Genetic correlation between a sire's phenotype and offspring variables**

Trait		Sire mating success		Sire size	
	n	r_G	*P*	r_G	*P*
Son mating success	4.7	**0.38**	**0.0076**	0.06	0.7679
Daughter reproductive	6.9	**– 0.36**	**0.0164**	−0.02	0.9280
Hatching*	545.9	0.01	0.9813	0.07	0.7549
Survivorship*	133.8	0.08	0.5708	0.03	0.8971
Son development*	21.2	−0.02	0.9134	0.01	0.9785
Daughter development*	23.8	0.03	0.8218	0.01	0.5381
Son size*	13.8	0.08	0.5924	0.17	0. 9670
Daughter size*	15.0	−0.16	0.2737	0.00	0.9990

* Juvenile viability variable.
Two sire phenotypes were examined, including sire mating success and sire size. *n* represents the average number of individuals per sire family. Bold values remain significant after a sequential Bonferroni. *P*-values corrected within each sire phenotype (mating success and size) and within each fitness stage (that is, adult fitness and juvenile viability).